energies

MDPI

Article

A Novel Synchrophasor Estimation Based on Enhanced All-Phase DFT with Iterative Compensation and Its Implementation

Zengqin Li [1], Weifeng Zhang [2], Zhiyuan Zhuang [2,*] and Tao Jin [2]

[1] China Railway Electric Industry Co., Ltd., Baoding 071051, China
[2] Department of Electrical Engineering and Automation, Fuzhou University, Fuzhou 350116, China
* Correspondence: zy.zhuang@foxmail.com

Abstract: Synchrophasor estimation was mostly used in transmission systems in the past, and it is difficult to directly apply an existing synchrophasor algorithm to a distribution system with a more complex structure and environment. A synchrophasor estimation algorithm with a high accuracy and fast response speed is required to complete the calculation of the phasor in the face of the complex and changeable power signal of a distribution network. Therefore, an enhanced all-phase discrete Fourier transform (e-apDFT) algorithm is proposed for a distribution system in this paper, and the algorithm is deployed in a phasor measurement unit (PMU) prototype based on digital signal processing (DSP). Aiming to solve the problem of the accuracy of the traditional apDFT being reduced when the response speed is fast due to the influence of a dense spectrum, the existing algorithm is improved through iteratively compensating the spectral interferences to the main bin produced by adjacent bins. The experimental results show that the e-apDFT algorithm still has a fast response speed and that its estimation accuracy is much better than that of the traditional apDFTs in the presence of adjacent harmonic components. The proposed algorithm also complies with the IEEE standards for P-class PMUs.

Keywords: all-phase DFT (apDFT); synchrophasor estimation; phasor measurement unit (PMU); iterative compensation

Citation: Li, Z.; Zhang, W.; Zhuang, Z.; Jin, T. A Novel Synchrophasor Estimation Based on Enhanced All-Phase DFT with Iterative Compensation and Its Implementation. *Energies* **2022**, *15*, 6964. https://doi.org/10.3390/en15196964

Academic Editor: Wei-Hsin Chen

Received: 21 July 2022
Accepted: 26 August 2022
Published: 23 September 2022

1. Introduction

Phasor measurement is an important means of support for state monitoring, protection, and the control of a whole power system. In the past, phasor measurement technology has been more widely used in the transmission network of a power system because of the existing technology and demand [1]. However, with the proposal and application of an active distribution network and other schemes, more attention has been paid to the phasor-based measurement of distribution systems [2]. The new distribution network, with its more complex state and structure and a great deal of distributed generation (DG), puts forward higher requirements on phasor-measurement technology [3], which not only has a higher accuracy, but also a faster response speed and strong anti-harmonic/noise capability. Therefore, finding a better synchrophasor estimation algorithm will be helpful for power systems' protection and control [4].

At present, there is a great deal of research on synchrophasor estimation, and new algorithms have been put forward with different results. Although the Kalman filter [5,6], least square algorithm [7,8], maximum likelihood algorithm [9,10], dynamic phasor model algorithm [11–13], wavelet transform algorithm [14], and other algorithms are widely used, they possess many shortcomings that make them unusable in practice. The discrete Fourier transform (DFT) algorithm is the most commonly used algorithm in signal processing. However, the incoherent sampling caused by frequency offset leads to spectral leakage. Therefore, in view of this problem, researchers have improved and developed algorithms

such as the interpolated DFT (IpDFT) [15–17]. These improvements are mainly based on the choice of window functions [18], the number of frequency bins [19,20], and spectral compensation [21,22]. In addition, in [23], an optimized combined cosine self-convolution window was applied to a synchrophasor-estimation algorithm.

The all-phase spectrum analysis technology was first proposed and used in image processing by Zhaohua Wang's team. Subsequently, it was readily applied to harmonic analysis [24,25], signal processing [26], and other fields due to its superior ability to suppress spectral leakage and unique phase invariance. This technology improves the spectral leakage problem of traditional DFTs from a new perspective and has a higher accuracy in phase estimation. Similarly, this method is also very suitable for the study of synchrophasor estimation. For example, the all-phase-mixed radix FFT algorithm proposed in [27] exhibits a higher accuracy than traditional algorithms. Reference [28] pushes further, introducing frequency offset compensation when the frequency offset is large, and uses windowless apFFT for frequency estimation so that high-precision estimation results can be obtained even when the frequency offset is large. However, the above studies failed to consider the influence of adjacent harmonics on the estimation results when the algorithm response speed is fast (low frequency resolution). At this time, although apDFT has an inhibitory effect on spectral leakage, the adverse effects of spectral interference cannot be ignored.

This paper conducts an in-depth study of an all-phase DFT (apDFT). It is found that in synchrophasor estimation, due to the high demand for response speed, the spectrum of the apDFT is denser, and the main bin is susceptible to interference from adjacent frequency bins. Once the signal has a DC component or a second harmonic component, the estimation accuracy is greatly reduced, which greatly affects the application of the apDFT algorithm in practice. In view of this limitation, this paper proposes an enhanced apDFT algorithm, combined with the time-shift phase difference correction (TSPDC) method, which iteratively compensates the spectral interference according to the spectral interference rate of the main bin and the adjacent frequency bins. Compared with the traditional apDFT algorithm, the proposed algorithm can overcome dense spectral interference and has a higher estimation accuracy.

The structure of this paper is as follows: Section 2 introduces the theoretical background of the apDFT spectrum analysis and the traditional apDFT algorithm. Section 3 deduces the formula of the proposed e-apDFT algorithm and emphasizes the selection of the algorithm parameters. Section 4 analyzes the proposed algorithm and comparison algorithms in static and dynamic simulation tests, as specified in [29], to verify the performance of each algorithm. Section 5 demonstrates the feasibility of the proposed algorithm through experiments. Finally, Section 6 concludes this paper with final remarks.

2. Principle of All-Phase DFT Spectrum Analysis

2.1. Theoretical Background

Data truncation of the signal sequence is the cause of the deterioration of the signal-processing result. The traditional DFT algorithm truncates the test point and $N-1$ points after this point for the DFT calculation, containing only one type of truncation. The data preprocessing part of the apDFT truncates the test point and the $N-1$ points before and after each time, including all the truncation types of the test point, which effectively suppresses the adverse consequences caused by data truncation. Figure 1 is a data preprocessing diagram of the apDFT.

The key component of the data preprocessing of the apDFT is the use of a convolution window. In Figure 1, $w_c(n)$ is a convolution window with a length of $2N-1$, which is formed by the convolution of two windows of length N, $w_1(n)$, and $w_2(n)$. According to the difference between the windows, all-phase data preprocessing can be divided into three categories: double rectangular ($w_1(n)$ and $w_2(n)$ are rectangular windows), single rectangular (only one of $w_1(n)$ and $w_2(n)$ is a rectangular window), and non-rectangular (neither $w_1(n)$ nor $w_2(n)$ are rectangular windows). In general, the effect of the non-rectangular all-phase data preprocessing is the best among the three.

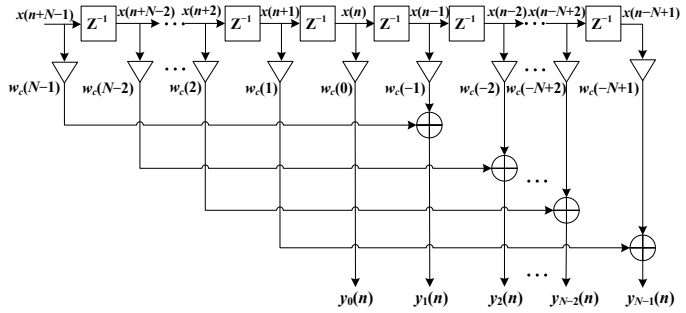

Figure 1. Data preprocessing diagram of apDFT.

Once the data preprocessing is completed, the N-point data are obtained and can be used as the input signal of the DFT, which is the same as the classical DFT. However, the result will have the ability to suppress spectral leakage and "phase invariance." Unlike with the traditional DFT, the phase of the apDFT has nothing to do with the frequency offset and is always the original phase of the signal, which can be considered as the main advantage of the apDFT. This characteristic is known as "phase invariance." Moreover, the apDFT's amplitude is the square of the traditional DFT's, which increases the gap between the main frequency bin and other bins and can suppress spectral leakage.

2.2. Traditional apDFT Algorithm Formulation

The object of the synchrophasor estimation is the power grid signal, whose standard discrete expression is:

$$x(n) = A\cos(2\pi f n T_s + \varphi_0) = A\cos(2\pi n\beta/N + \varphi_0) \tag{1}$$

where A, f, and φ_0 are the amplitude, frequency, and phase of the signal, respectively. T_s is the sampling period; $T_s = 1/f_s$, where f_s is the sampling frequency.

In this paper, the triangular window is selected as the window function for the all-phase data preprocessing, because it can improve the accuracy of the algorithm while ensuring real-time performance.

The triangular window can be represented in the time domain as:

$$w(n) = \begin{cases} \frac{2n+1}{N} & 0 \le n \le \frac{N}{2} - 1 \\ 2 - \frac{2n+1}{N} & \frac{N}{2} \le n \le N - 1 \end{cases} \tag{2}$$

where $n = 0, 1, 2, \ldots, N-1$. The amplitude spectrum function of the triangular window is:

$$W(\omega) = \frac{2}{N}\left[\frac{\sin(\omega N/4)}{\sin(\omega/2)}\right]^2 e^{-j(\frac{N}{2}-1)\omega} \tag{3}$$

The calculation formula of the apDFT with double windows can be obtained from:

$$X(k) = Ae^{-j\varphi_0}W^2(\omega - \omega^*) \tag{4}$$

where $\omega = 2\pi k/N$, $\omega^* = 2\pi\beta/N$, and $\beta = f/f_0$; the frequency resolution of the algorithms discussed in this paper is uniformly the nominal frequency f_0, and N is a number of samples in one period. For a symmetric window, the spectrum function obtained by convolution is the real spectrum, and the phase spectrum is zero.

By performing the apDFT on (1), the spectrum function can be obtained as:

$$X_{ap}(k) = \frac{A}{2}\left\{e^{-j\varphi_0}W^2[2\pi(k-\beta)/N] + e^{j\varphi_0}W^2[2\pi(k-\beta)/N]\right\} \tag{5}$$

Although the apDFT can obtain the high-precision phase and has a spectral leakage suppression capability, the influence of spectral leakage still exists, such that the frequency and amplitude of the fundamental tone still need to be obtained through spectrum correction. Consequently, this paper adopts the time-shift phase difference correction method because of its high spectrum-correction accuracy.

The TSPDC method requires two groups of samples. The first $2N-1$ samples are taken as the first subsequence, and the second $2N-1$ samples are taken as the second subsequence. The ApDFT is run to obtain the phase of the main tone, φ_1 and φ_2.

(1) Phase estimation: Since the accuracy of the phase obtained by the apDFT is high enough that no further correction is required, the value of the phase estimation is φ_1.

(2) Frequency estimation: Theoretically, the relation between the phase difference of two subsequences and the frequency is:

$$\Delta\varphi = \varphi_2 - \varphi_1 = 2\pi\beta n_0/N \tag{6}$$

where n_0 is the number of sampling intervals between the first sequence and the second sequence. Due to the characteristics of the algorithm, the phase difference $\Delta\varphi$ is limited within $[-2\pi, 2\pi]$, which is called "phase ambiguity". In order to solve this problem, we need to correct the phase difference:

$$\Delta\varphi = 2\pi\beta n_0/N - 2\pi n_0/N \tag{7}$$

where the default frequency resolution is the nominal frequency f_0 of the power grid. According to the above formula, the frequency offset rate is:

$$\hat{r} = \frac{\Delta\varphi N}{2\pi n_0} \tag{8}$$

Thus, the estimated frequency can be obtained as:

$$\hat{f} = (1+\hat{r})f_0 \tag{9}$$

The rate of change of frequency (*ROCOF*) is:

$$ROCOF = \frac{df}{dt} = \frac{\Delta f}{\triangle nT_s} \tag{10}$$

In discrete computation, the expression is the first order difference of frequency.

(3) Amplitude estimation: Combine (2), (5), and (9):

$$\hat{A} = 2\left|X_{ap}(k_0)\right| / \left|\frac{N^2}{4}\left(\frac{\sin(\hat{r}\pi/2)}{\hat{r}\pi/2}\right)^4\right| \tag{11}$$

Aiming at the incomputable situation where $\hat{r}$ is close to zero, curve fitting is carried out for the division section:

$$\frac{\hat{r}\pi/2}{\sin(\hat{r}\pi/2)} = 0.0200448\cdot|\hat{r}|^7 + 0.0126921\cdot\hat{r}^6 + 0.0081678\cdot|\hat{r}|^5 + 0.1163573\cdot\hat{r}^4 + 0.4112145\cdot\hat{r}^2 + 1 \tag{12}$$

3. Proposed Enhanced-ApDFT

Although Section 2 mentions that the apDFT has the advantage of suppressing spectral leakage better than the ordinary DFT, due to the real-time requirement of synchrophasor estimation, its frequency resolution is lower, the bins of the fundamental tone and each harmonic are closer, and the mutual interference between them is greater. Consequently, the apDFT has some shortcomings that cannot be ignored.

The frequency resolution of the algorithms discussed in this paper is uniformly the nominal frequency f_0, so the fundamental tone is mainly affected by the adjacent compo-

nents (the DC component and the second harmonic component). As shown in Figure 2, the apDFT is performed on the fundamental tone, DC component, and second harmonic component. The results show that the three components affect each other in terms of spectral leakage, though when the distance exceeds two frequency resolutions, the effect of the spectral leakage is negligible. In this case, once there is a DC component or second harmonic component in the power signal, which is inevitable, the estimation accuracy of the apDFT is greatly reduced.

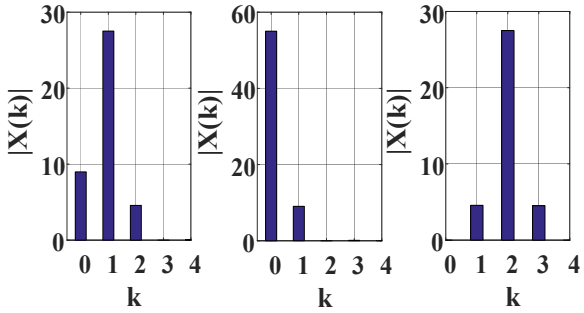

Figure 2. ApDFT results of the fundamental, DC, and second harmonic components.

The proposed e-apDFT algorithm can be used to estimate and compensate for the effect of spectral leakage caused by the DC component and the second harmonic. In order to achieve this goal, the degree of the spectral leakage of each component on two observable, adjacent apDFT bins needs to be obtained. More specifically, their ratio, which is called the spectral interference rate, δ, in this paper, should be calculated. The apDFT results are divided into the real spectrum and the imaginary spectrum, and the corresponding spectral interference rates are denoted as δr and δi, respectively. A conclusion is drawn by analyzing the apDFT results of a large number of signals with different amplitudes, frequencies, and phases; when the frequency is fixed, δr and δi are constant (as shown in Figure 3). According to this conclusion, the interference caused by the DC component and the second harmonic component can be analyzed independently.

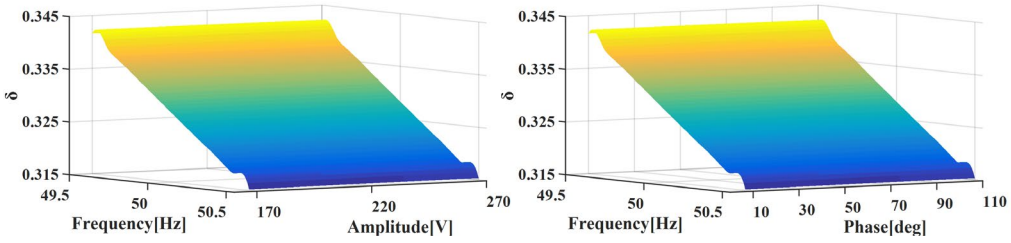

Figure 3. The relation between the spectral interference rate and phasor.

(1) DC component: As is well known, the frequency of a power grid signal fluctuates within a certain range, and the spectral interference rate changes with the frequency fluctuation. As such, the apDFT is carried out for a group of single-tone power grid signals with different frequencies, and the corresponding group of spectral interference rates δr and δi are calculated. The expression of the relation between the spectral interference rate and the frequency of the power grid can be obtained by fitting this curve:

$$\delta r_1 = -0.0262735f + 1.642020 \tag{13}$$

where δ_{r1} is the spectral interference rate of the real spectrum between the bin of the DC component and the main bin. At the same time, the imaginary spectrum of the DC component is always zero, so it is unnecessary to calculate the spectral interference rate of the imaginary spectrum. The above results all take the negative image of the spectrum

into account because the interference of the main tone and its negative image to the DC component is the same.

Given the expression of the spectral interference rate, the interference caused by the DC component can be estimated and compensated. First, the frequency f is obtained according to the traditional apDFT, and δr_1 is obtained by (12). Then, the real spectral leakage of the fundamental tone of the DC component is obtained by the following equation:

$$\hat{X}_{1-0} = real\left[X_{ap}(1)\right] \times \delta r_1 \tag{14}$$

where $X_{ap}(1)$ is the main apDFT bin of the spectrum. Although the apDFT bins calculated are biased in the presence of other interfering tones, they can still be used to approximate the true value in the first calculation and then corrected in the subsequent iterative compensation, at which point the true apDFT result of the DC component is obtained:

$$\widetilde{X}_{ap}(0) = X_{ap}(0) - 2\hat{X}_{1-0} \tag{15}$$

In addition, the real spectral leakage of the DC component of the main bin is obtained:

$$\hat{X}_{0-1} = \widetilde{X}_{ap}(0) \times \delta r_1{}' \tag{16}$$

Finally, we can obtain the modified main bin value:

$$\widetilde{X}_{ap}(1) = X_{ap}(1) - \hat{X}_{0-1} \tag{17}$$

(2) Second harmonic component: An ApDFT is also carried out for a group of single-tone power grid signals at different frequencies. Based on the results, the spectral interference rates, δr_2 and δi_2, are calculated. The expression of the relation between the spectral interference rate and the frequency of the power grid can be obtained by fitting these curves:

$$\delta r_2 = 0.013064f - 0.487009 \tag{18}$$

$$\delta i_2 = 0.013209f - 0.498301 \tag{19}$$

The estimated frequency f is also obtained according to the traditional apDFT, and then δ_{r2} and δ_{i2} are obtained by (17) and (18). The interference is estimated and compensated according to the following equations:

$$\hat{X}r_{1-2} = real\left[X_{ap}(1)\right] \times \delta r_2 \tag{20}$$

$$\hat{X}i_{1-2} = imag\left[X_{ap}(1)\right] \times \delta i_2 \tag{21}$$

$$\widetilde{X}_{ap}(2) = X_{ap}(2) - \hat{X}r_{1-2} - i \times \hat{X}i_{1-2} \tag{22}$$

$$\hat{X}r_{2-1} = real\left[\widetilde{X}_{ap}(2)\right] \times \delta r_2{}' \tag{23}$$

$$\hat{X}i_{2-1} = imag\left[\widetilde{X}_{ap}(2)\right] \times \delta i_2{}' \tag{24}$$

$$\widetilde{X}_{ap}(1) = X_{ap}(1) - \hat{X}r_{2-1} - i \times \hat{X}i_{2-1} \tag{25}$$

In short, it is only necessary to combine the estimation and compensation of the interference of the DC component and the second harmonic. Here, we can accomplish both parts at the same time, thus improving the estimation accuracy of the traditional apDFT. After the estimation and compensation calculation, a result with a higher accuracy is obtained. Theoretically, through iterative calculation, a result with an even smaller error can be obtained, so we replace the initial result with the obtained result and perform the compensation calculation again.

In order to determine the optimal number of iterations, we iteratively estimate and compensate the power signal affected by the DC component and second harmonic, respectively, and obtain the errors of the real and imaginary parts of the main bin, as shown in Figure 4. It is evident that if the number of iterations exceeds three, the errors are almost constant. Hence, in order to reduce unnecessary calculations, it is appropriate to select the number of iterations as three.

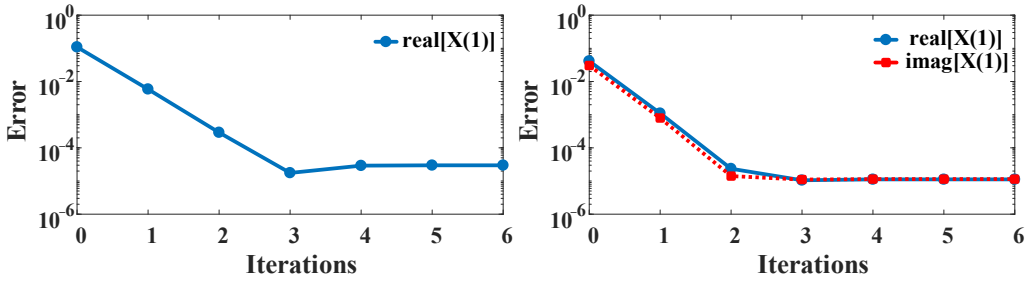

Figure 4. The estimation error of the main bin under different iterations.

At the same time, the e-apDFT algorithm should only start iterative compensation when the DC component and the second harmonic component exist. Otherwise, it not only increases the computational complexity, but also reduces the estimation accuracy. Therefore, thresholds must be set to determine whether to initiate an iterative compensation. Here, we choose $\widetilde{X}_{ap}(0)$ from (14) as the criterion of the iterative compensation of the DC component:

$$S_1 = \frac{\left|\widetilde{X}_{ap}(0)\right|}{\left|X_{ap}(1)\right|} > \lambda_1 \tag{26}$$

where λ_1 is the threshold for starting the iterative compensation part of the DC component. Meanwhile, the real and imaginary parts of (21) are selected as the criteria of the second harmonic component:

$$S_2 = \max\left(\frac{\left|real\left(\widetilde{X}_{ap}(2)\right)\right|}{\left|X_{ap}(1)\right|}, \frac{\left|imag\left(\widetilde{X}_{ap}(2)\right)\right|}{\left|X_{ap}(1)\right|}\right) > \lambda_2 \tag{27}$$

where λ_2 is the threshold for starting the iterative compensation part of the second harmonic component.

The determination of the thresholds, λ_1 and λ_2, should also be considered to avoid the false start of the iterative compensation caused by dynamic events. As such, apDFT calculations under different dynamic events are performed to obtain the maximum values of S_1 and S_2, as shown in Figure 5. Since the step event in the dynamic event has a strong change in an instant, the influence caused by the false start of the iterative compensation can be ignored at this time; thus, the threshold can be determined without considering the step event. It is evident from Figure 5 that for the iterative compensation program to avoid starting erroneously during dynamic events, the thresholds λ_1 and λ_2 must be greater than 5.25×10^{-3} and 2.92×10^{-3}, respectively. Taking these margins into full consideration, this paper selects 0.006 and 0.004 as the values of λ_1 and λ_2.

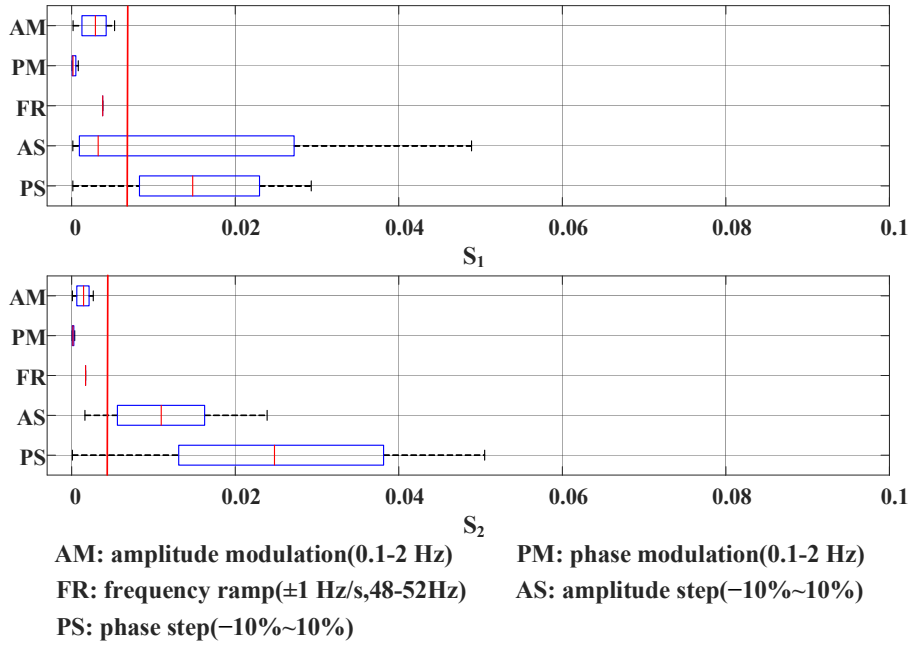

Figure 5. Boxplot representation of S1 (**top**) and S2 (**bottom**) in all dynamic events.

4. Simulation Analysis

Based on the IEEE standards [29], the simulation analysis carries out static and dynamic tests on the proposed e-apDFT algorithm. The simulation results are mainly presented through three indicators: the frequency error (FE), the rate of change of frequency error (RFE), and the total vector error (TVE). The error limits of P- and M-class PMUs are given. In addition, two other algorithms are tested under the same conditions for comparison against the performance of the proposed algorithm. The two comparison algorithms are the (1) non-rectangular apDFT based on a Hanning window (hann-apDFT), and (2) the non-rectangular apDFT based on a triangular window (triang-apDFT). The simulation parameters are shown in Table 1.

Table 1. Algorithm parameters.

Variable	Parameter	Value
f_0	Nominal frequency	50 Hz
L	Window length	$2N-1$ (N = 64)
f_s	Sampling rate	3.2 kHz
f_r	Resolution	50 Hz
F_r	Reporting rate	50 fps
N_I	Iterations	3

4.1. Static Tests

First, a single tone signal with a frequency ranging from 45 Hz–55 Hz (frequency offset ± 5 Hz) was tested. The maximum phasor error results are shown in Figure 6.

It is evident from Figure 6 that the apDFT algorithms have a very high estimation accuracy at the nominal frequency of the power grid and that the estimation error increases with the increase in the frequency offset. Although the FE and RFE of the hann-apDFT exceeded the error limit of the IEEE standard with the increase in the frequency offset, the triang-apDFT algorithm and the e-apDFT algorithm are always within the error limit. Since there is no DC component and no second harmonic component, the iterative compensation is not initiated, so the results of the two apDFT algorithms are completely consistent.

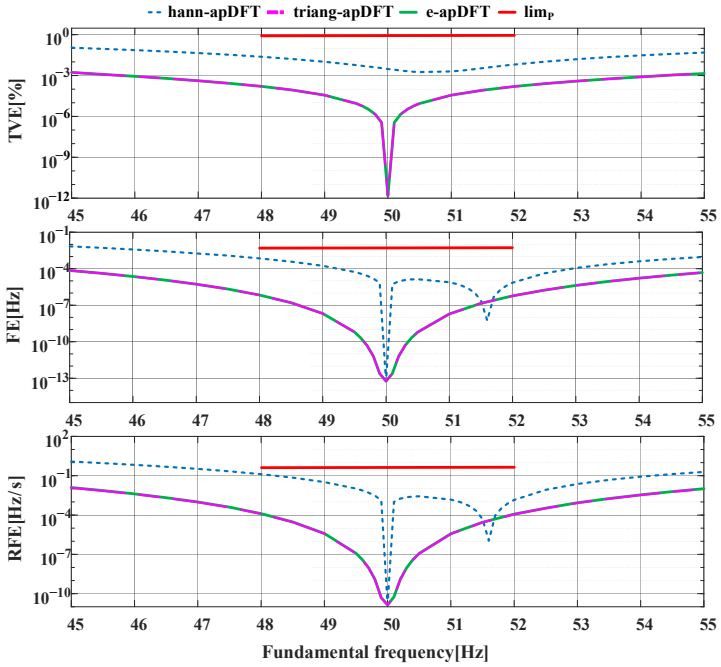

Figure 6. Signal frequency range test.

Next, the harmonic distortion test is carried out. The frequency of the test signal is offset by 0.5 Hz, with a single harmonic. From the 2nd to the 50th harmonic, the amplitude is 1% of the fundamental amplitude. The maximum phasor error results are shown in Figure 7. As shown, the estimation error of the hann-apDFT algorithm is relatively stable, whereas the apDFT algorithms based on a triangular window are greatly affected by even harmonics. Even so, overall, the latter have a higher estimation accuracy. The key observation is that when the second harmonic exists, the phasor estimation accuracy of the hann-apDFT algorithm and the triang-apDFT algorithm is greatly reduced, while the e-apDFT maintains a high accuracy.

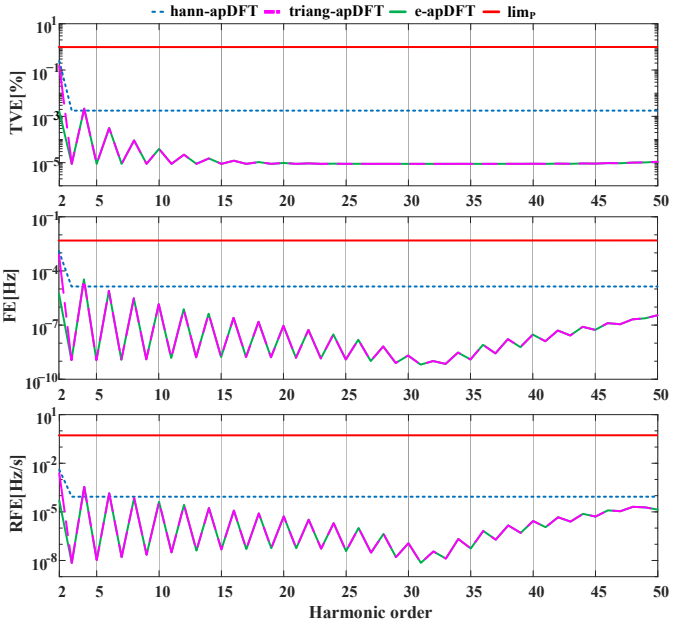

Figure 7. Harmonic distortion test (THD = 1%).

In order to better demonstrate the difference between the proposed algorithm and the traditional algorithm, the real-time simulation results of the following two cases are given: (1) a single tone signal with a DC component of 1%, and (2) a single tone signal with a second harmonic component of 1%.

It can be seen from Figure 8 that the two comparison algorithms are seriously affected by the DC component and the second harmonic, and their FE and TVE all approximate the specified error limit. On the other hand, the proposed e-apDFT algorithm reduces the errors by two to three orders of magnitude due to the addition of iterative compensation procedures. This difference indicates that the enhanced apDFT algorithm used in this paper is effective. Furthermore, this advantage will become more obvious as the proportion of the harmonics increases.

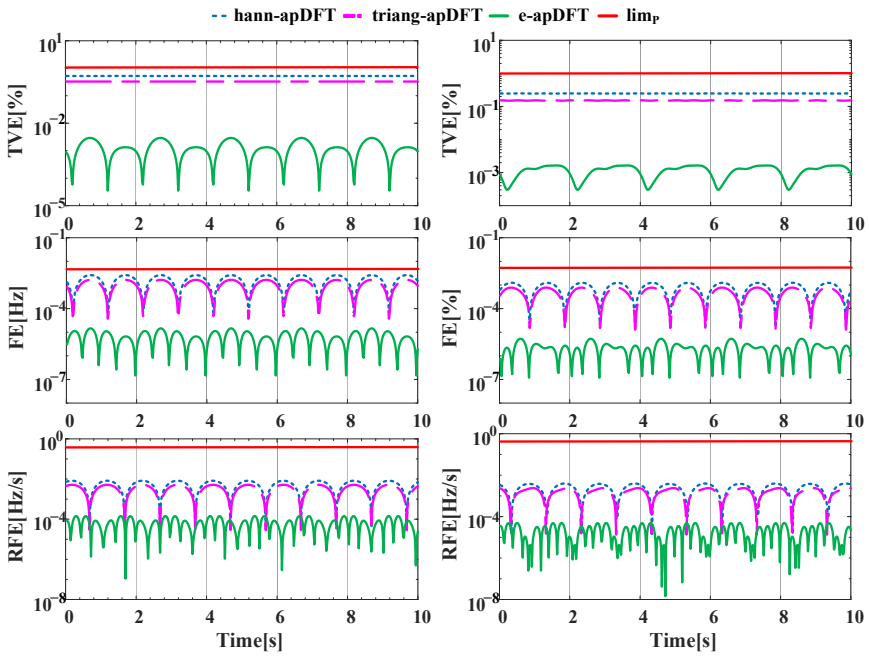

Figure 8. The interference of the DC component and the second harmonic.

4.2. Dynamic Tests

Dynamic tests can simulate complex situations that arise under actual working conditions. Therefore, in addition to the related static tests, the algorithm should also be performed for the specified dynamic tests. In other words, the algorithm is feasible only if it meets both the static and dynamic test requirements. The dynamic tests mainly include the following three parts: (1) the measurement bandwidth, (2) frequency ramp, and (3) amplitude and phase steps.

The measurement bandwidth is divided into amplitude modulation and phase modulation, whose test signals are as follows:

$$x(t) = A_0[1 + k_x \cos(2\pi f_m t)] \times \cos[2\pi f_0 t + k_a \cos(2\pi f_m t - \pi)] \quad (28)$$

where A_0 is the amplitude of the input signal; f_0 is the fundamental frequency of the power system; f_m is the modulation frequency, which has a range of [0.1, 2] Hz; k_x is the amplitude modulation coefficient; and k_a is the phase modulation coefficient. For the amplitude modulation, $k_x = 0.1$ and $k_a = 0$; for the phase modulation, $k_x = 0$ and $k_a = 0.1$.

Figure 9 is the result of the amplitude modulation test. It is evident that as the modulation frequency increases, the FE, RFE, and TVE of the three algorithms also gradually increase, though they are far less than the error limit in [29]. Moreover, the FE and RFE of the proposed e-apDFT algorithm are always significantly less than those of the hann-apDFT algorithm, while the TVE of the proposed algorithm changes from less than to close to that

of the hann-apDFT as the modulation frequency increases. It is worth noting that due to the threshold setting, the iterative compensation part of the e-apDFT algorithm will not erroneously start due to the occurrence of dynamic events, so the results obtained by the e-apDFT across all the dynamic tests are exactly the same as those of the triang-apDFT.

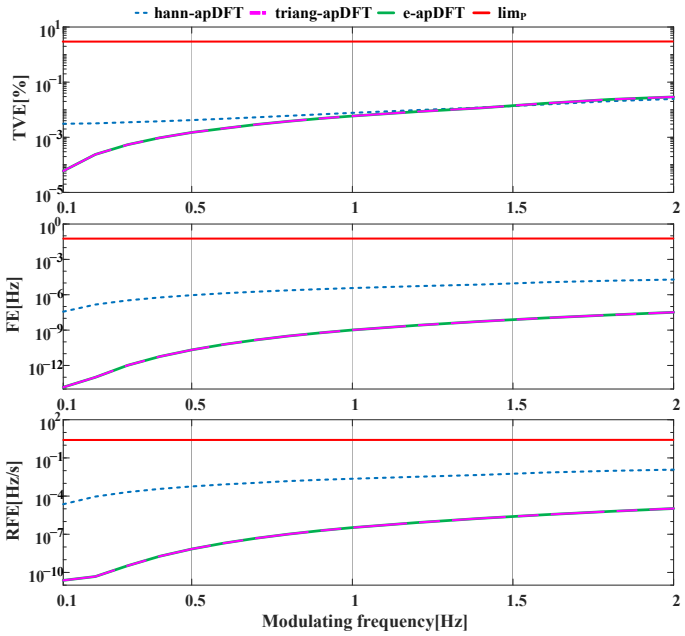

Figure 9. Amplitude modulation test.

Figure 10 shows the results of the phase modulation. The FE of the three algorithms is basically the same, and when the modulation frequency is low, the RFE and TVE of the e-apDFT algorithm are at most two orders of magnitude lower than those of the hann-apDFT algorithm. However, as the modulation frequency increases, the values are nearly the same.

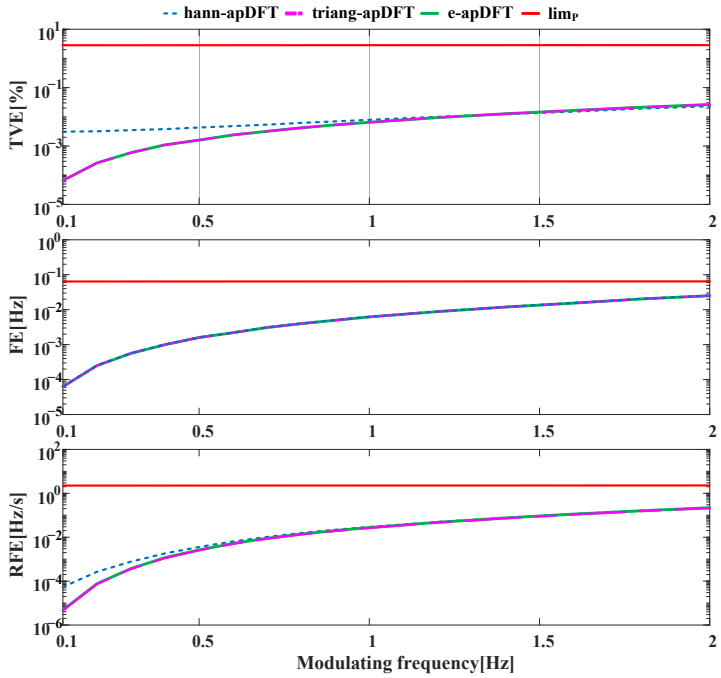

Figure 10. Phase modulation test.

A frequency ramp refers to the situation where the signal frequency changes at a rate of 1 Hz/s. It is divided into a positive ramp (positively increased from 48 Hz to 52 Hz) and a negative ramp (reduced from 52 Hz to 48 Hz). As can be seen from the results in Figure 11, the estimation error of the e-apDFT algorithm is always within the expected range, regardless of whether the frequency ramp is positive or negative, and its FE and TVE do not change with the instantaneous frequency. On the other hand, the errors of the hann-apDFT algorithm begins to increase when the instantaneous frequency is offset from the nominal frequency.

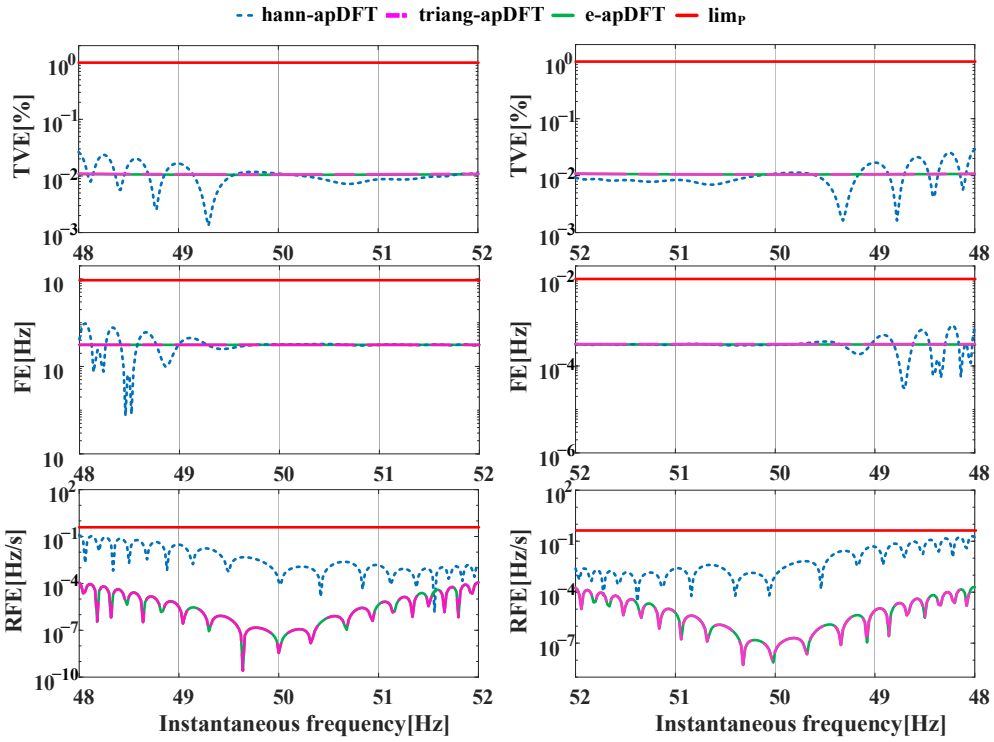

Figure 11. Frequency ramp test.

Finally, the step test is divided into an amplitude step and a phase step. This test mainly checks the stability and response time of the algorithm when it encounters a signal mutation.

For the amplitude step, the amplitude of the test signal (with a frequency of 50.5 Hz) increases by 10% at a certain time and is always accompanied by 60 dB of Gaussian white noise (though it is not explicitly required in [29]). Figure 12 shows that the three apDFT algorithms have almost the same response time due to having the same parameters, and all meet the standards of P- and M-class PMUs. That said, the estimation errors of the triang-apDFT algorithm and the e-apDFT algorithm before and after the mutation are much smaller than that of the hann-apDFT algorithm.

For the phase step, the phase of the test signal (with a frequency of 50.5 Hz), again accompanied by noise, suddenly increases by 10% at a certain moment. The result is similar to that of the amplitude step test, as shown in Figure 13. The response time and estimation errors of the proposed algorithm both meet the requirements of P- and M-class PMU standards and are better than those of the hann-apDFT algorithm.

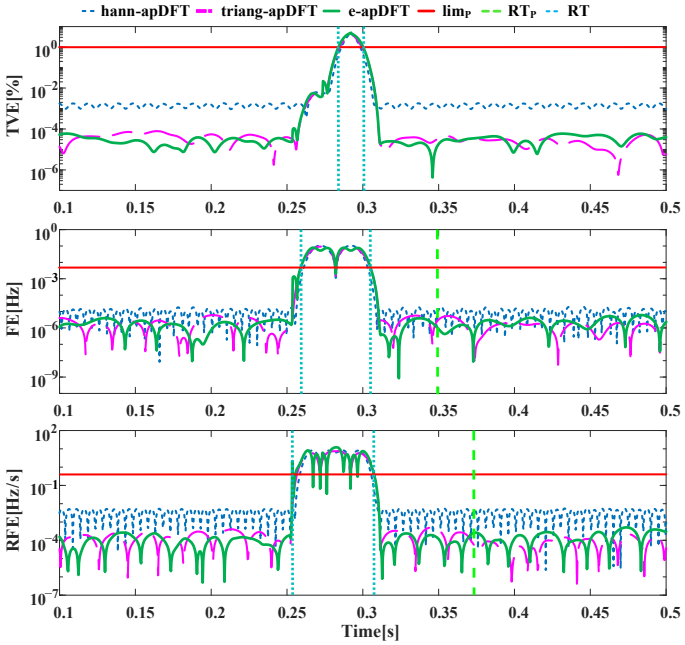

Figure 12. Amplitude ramp test.

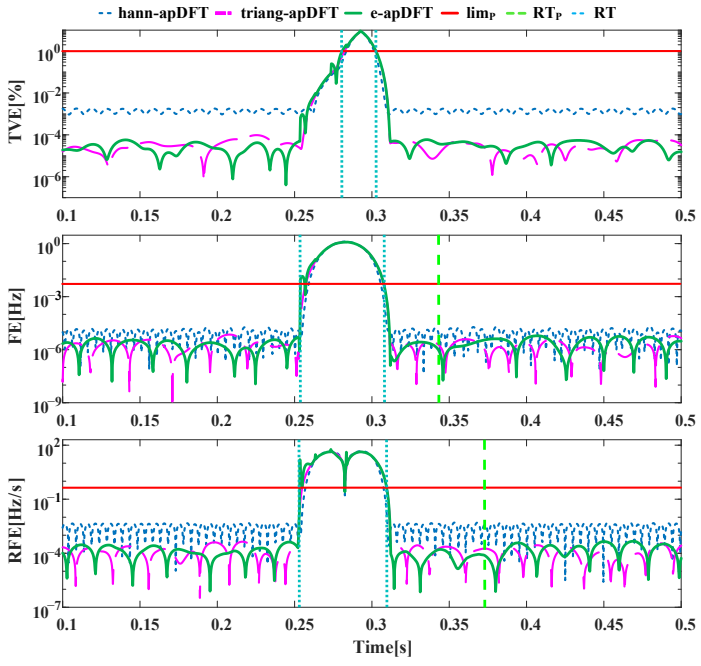

Figure 13. Phase step test.

5. Implementation in the DSP-Based Hardware Platform

In this section, the effectiveness of the proposed algorithm when used with a PMU prototype is proved through static and dynamic testing, fault testing, and other related experiments. In addition, we show that the algorithm proposed in this paper has a low computational complexity and a short computational time, and that the phasor measurement can be completed by using a low-cost DSP.

In practice, the measurement results of a PMU will be affected by many factors, such as the calculation accuracy, sampling accuracy, and environmental interference. Therefore, it is necessary to build a PMU prototype to verify the effectiveness of the proposed algorithm in practice. In this paper, a PMU prototype system based on a DSP is designed, and its

hardware structure is shown in Figure 14. The experimental system is mainly composed of the following four parts: (1) a synchronous clock module, namely, the ATK-S12126F8-BD dual-mode positioning module (GPS/BD), which can provide coordinated universal time (UTC) and pulse per second (PPS) for generating a synchronous sampling pulse; (2) a data acquisition module, which is composed of a second-order low-pass KRC filter circuit and an AD conversion module (AD7606), responsible for signal filtering and acquisition; (3) a data processing module, which is composed of TMS320F28335 (DSP1) and 2812 (DSP2), where DSP1 is responsible for phasor calculation and DSP2 is responsible for UTC analysis; and (4) a communication module, namely, the ATK-ESP8266 module, used for time and phasor transmission.

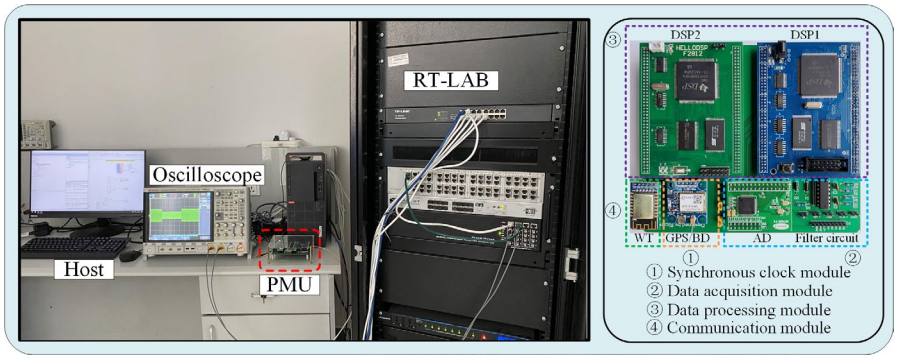

Figure 14. The experimental facilities (**left**) and PMU prototype hardware structure (**right**).

After the PMU prototype is built, the proposed algorithm is deployed on the prototype. Actual power grid signals or a programmable AC power supply can be used as input signal sources. RT-LAB is an industrial-grade experimental platform composed of hardware equipment (composed of CPU, FPGA, I/O boards, etc.) and supporting software packages. It can generate and output all the signals required by the IEEE standard, but a signal generator or AC power supply cannot do this. At the same time, it can run the distribution network model to output power signals during various faults. Thus, the RT-LAB is selected in this paper for a reference and comparison of the experimental results. The working process of the PMU prototype is as follows: The test signal (from RT-LAB) is filtered and limited (the phase lag is solved by an algorithm), and then sampled. The generation of the control signal of the sampling module, the reading of the sampling data, and the calculation of the proposed algorithm are executed by DSP1, and the time information from the synchronous clock module is obtained, analyzed, packed with the phasor information obtained from DSP1, and sent to the host computer by DSP2.

The proposed algorithm and prototype were also tested according to the test scenario setting in the IEEE standard. The results are shown in Tables 2 and 3 (the report rate of this experiment is 50/s). Table 2 shows the test results under static and dynamic scenarios, while Table 3 shows the response time results under the step tests. It is evident that in static and dynamic tests under the IEEE standard, a PMU prototype equipped with the algorithm proposed in this paper can achieve a high measurement accuracy, and the measurement results are all less than the specified error limit, fully meeting the measurement requirements of a P-class PMU.

A distribution network fault was simulated by RT-LAB in this experiment, and the relevant measurement results were recorded. The first is a single-phase grounding fault in the power distribution system. As shown in Figure 15, the distribution system was operating normally before the fault, and the estimation results of the phasors were highly accurate. When a fault occurs, the voltage drops to zero, and the frequency and phase estimates also fluctuate greatly. After the fault is cleared, the system returns to the steady state. The entire fault process is under the real-time monitoring of the PMU prototype, and the algorithm's accuracy is high.

Table 2. Measurement Results of the PMU Prototype under Static and Dynamic Tests.

Static/Dynamic Test	Parameter Setting	Max FE/Hz		Max RFE/(Hz/s)		Max TVE/%	
		Sta. [1]	Mea. [2]	Sta.	Mea.	Sta.	Mea.
Frequency offset	48~52 Hz	0.005	9.57×10^{-4}	0.4	0.10	1	0.0194
Harmonic distortion	Harmonic: 2~50th (1%)	0.005	0.0012	0.4	0.11	1	0.1018
Frequency ramp	±1 Hz/s (48~52 Hz)	0.01	0.0027	0.4	0.09	1	0.0832
Amplitude modulation	Modulation frequency: 0~2 Hz	0.06	8.66×10^{-4}	2.3	0.11	3	0.0231
Phase modulation	Modulation frequency: 0~2 Hz	0.06	0.0251	2.3	0.99	3	0.0925

[1] "Sta." = Standard value; [2] "Mea." = Measured value.

Table 3. Response Times under the Step Test.

Step Test	RT_{FE}/s		RT_{RFE}/s		RT_{TFE}/s	
	Sta.	Mea.	Sta.	Mea.	Sta.	Mea.
AS	$4.5/f_0$	$2.6/f_0$	$6/f_0$	$3.1/f_0$	$2/f_0$	$0.8/f_0$
PS	$4.5/f_0$	$2.7/f_0$	$6/f_0$	$3.0/f_0$	$2/f_0$	$1.2/f_0$

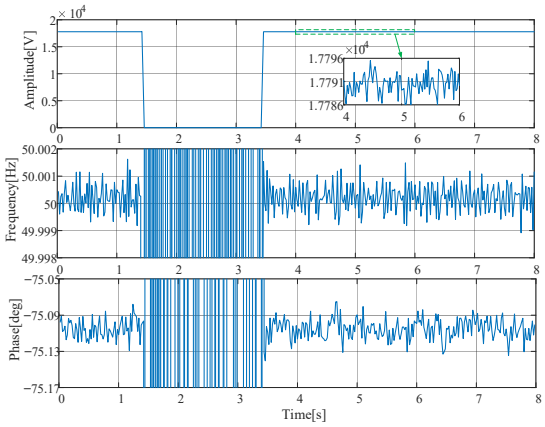

Figure 15. Measurement results of the PMU prototype under single-phase grounding fault.

In addition, the load-switching test of the power distribution system was also carried out. The results are shown in Figure 16. When the distribution system is in normal operation, a load leaves for a period of time and then rejoins the system. It is evident that the PMU prototype on the node closest to the load effectively monitors the change in the phasor during the load switching process. In addition, its estimation accuracy is always high.

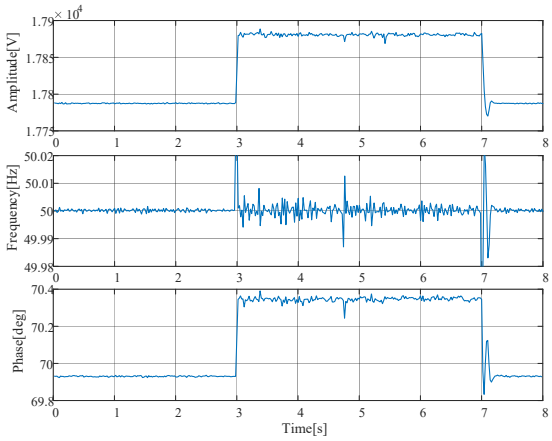

Figure 16. Measurement results of the PMU prototype under load switching.

6. Conclusions

In this paper, an enhanced apDFT algorithm was proposed to solve the problem of the accuracy of the traditional apDFT algorithm being greatly reduced due to dense frequency bins and the influence of adjacent harmonics. By means of iterative compensation, the spectral leakage of the adjacent harmonics was effectively suppressed, and the accuracy of the synchrophasor estimation was improved. The main contributions of the proposed algorithm are: (1) The error estimation and iterative compensation in this paper are different from existing algorithms. The e-apDFT uses a curve-fitting method, and the final number of iterations is less. (2) This paper improves the all-phase DFT and solves the problems of the traditional apDFT applications in the synchrophasor measurement field. (3) The selection of the judgment index and thresholds of the iterative compensation are more effective and practical.

In this paper, static and dynamic simulation analysis of the proposed algorithm were carried out according to IEEE-related standards. The results show that the proposed algorithm compensates for the deficiency of the traditional apDFT algorithm and fully meets the relevant standards. At the same time, a PMU prototype based on the DSP was constructed through experiments, and the proposed algorithm was deployed within it. Static and dynamic tests and fault simulation tests were then conducted to prove the feasibility of the proposed algorithm in the actual phasor estimation.

Author Contributions: Supervision, T.J.; Writing—original draft, W.Z.; Writing—review & editing, Z.L. and Z.Z. All authors have read and agreed to the published version of the manuscript.

Funding: This research received no external funding.

Institutional Review Board Statement: Not applicable.

Informed Consent Statement: Not applicable.

Data Availability Statement: Not applicable.

Conflicts of Interest: The authors declare no conflict of interest.

References

1. Bhatt, N.B. Role of Synchrophasor Technology in the Development of A Smarter Transmission Grid. In Proceedings of the IEEE PES General Meeting, Providence, RI, USA, 25–29 July 2010.
2. Dusabimana, E.; Yoon, S. A Survey on the Micro-Phasor Measurement Unit in Distribution Networks. *Electronics* **2020**, *9*, 305. [CrossRef]
3. Akrami, A.; Doostizadeh, M.; Aminifar, F. Optimal Reconfiguration of Distribution Network Using μPMU Measurements: A Data-Driven Stochastic Robust Optimization. *IEEE Trans. Smart Grid* **2020**, *11*, 420–428. [CrossRef]
4. Fu, L.; Yu, L.; Xiong, S.; He, Z.; Mai, R.; Li, X. A Dynamic Synchrophasor Estimation Algorithm Considering Out-of-Band Interference. *IEEE Trans. Power Deliv.* **2022**, *37*, 1193–1202. [CrossRef]
5. Huang, C.; Xie, X.; Jiang, H. Dynamic Phasor Estimation Through DSTKF Under Transient Conditions. *IEEE Trans. Instrum. Meas.* **2017**, *66*, 2929–2936. [CrossRef]
6. Ferrero, R.; Pegoraro, P.A.; Toscani, S. Synchrophasor Estimation for Three-Phase Systems Based on Taylor Extended Kalman Filtering. *IEEE Trans. Instrum. Meas.* **2020**, *69*, 6723–6730. [CrossRef]
7. Kim, J.; Kim, H.; Choi, S. Performance Criterion of Phasor Measurement Units for Distribution System State Estimation. *IEEE Access* **2019**, *7*, 106372–106384. [CrossRef]
8. Rao, A.V.K.; Soni, K.M.; Sinha, S.K.; Nasiruddin, I. Accurate phasor and frequency estimation during power system oscillations using least squares. *IET Sci. Meas. Technol.* **2019**, *13*, 989–994.
9. Oubrahim, Z.; Choqueuse, V.; Amirat, Y.; Benbouzid, M.E.H. Maximum-Likelihood Frequency and Phasor Estimations for Electric Power Grid Monitoring. *IEEE Trans. Ind. Inform.* **2018**, *14*, 167–177. [CrossRef]
10. Choqueuse, V.; Belouchrani, A.; Auger, F.; Benbouzid, M. Frequency and Phasor Estimations in Three-Phase Systems: Maximum Likelihood Algorithms and Theoretical Performance. *IEEE Trans. Smart Grid* **2019**, *10*, 3248–3258. [CrossRef]
11. Vejdan, S.; Sanaye-Pasand, M.; Malik, O.P. Accurate Dynamic Phasor Estimation Based on the Signal Model Under Off-Nominal Frequency and Oscillations. *IEEE Trans. Smart Grid* **2017**, *8*, 708–719. [CrossRef]
12. Bi, T.; Liu, H.; Feng, Q.; Qian, C.; Liu, Y. Dynamic Phasor Model-Based Synchrophasor Estimation Algorithm for M-Class PMU. *IEEE Trans. Power Deliv.* **2015**, *30*, 1162–1171. [CrossRef]

13. Narduzzi, C.; Bertocco, M.; Frigo, G.; Giorgi, G. Fast-TFM—Multifrequency Phasor Measurement for Distribution Networks. *IEEE Trans. Instrum. Meas.* **2018**, *67*, 1825–1835. [CrossRef]
14. Chauhan, K.; Reddy, M.V.; Sodhi, R. A Novel Distribution-Level Phasor Estimation Algorithm Using Empirical Wavelet Transform. *IEEE Trans. Ind. Electron.* **2018**, *65*, 7984–7995. [CrossRef]
15. Serbes, A. Fast and Efficient Sinusoidal Frequency Estimation by Using the DFT Coefficients. *IEEE Trans. Commun.* **2019**, *67*, 2333–2342. [CrossRef]
16. Frigo, G.; Derviskadic, A.; Paolone, M. Reduced Leakage Synchrophasor Estimation: Hilbert Transform Plus Interpolated DFT. *IEEE Trans. Instrum. Meas.* **2019**, *68*, 3468–3483. [CrossRef]
17. Sun, Y.; Zhuang, C.; Xiong, Z. A Switch-Based Interpolated DFT for the Small Number of Acquired Sine Wave Cycles. *IEEE Trans. Instrum. Meas.* **2016**, *65*, 846–855. [CrossRef]
18. Macii, D.; Petri, D.; Zorat, A. Accuracy Analysis and Enhancement of DFT-Based Synchrophasor Estimators in Off-Nominal Conditions. *IEEE Trans. Instrum. Meas.* **2012**, *61*, 2653–2664. [CrossRef]
19. Wen, H.; Li, C.; Tang, L. Novel Three-Point Interpolation DFT Method for Frequency Measurement of Sine-Wave. *IEEE Trans. Ind. Inform.* **2017**, *13*, 2333–2338. [CrossRef]
20. Wen, H.; Li, C.; Yao, W. Power System Frequency Estimation of Sine-Wave Corrupted with Noise by Windowed Three-Point Interpolated DFT. *IEEE Trans. Smart Grid* **2018**, *9*, 5163–5172. [CrossRef]
21. Romano, P.; Paolone, M. Enhanced Interpolated-DFT for Synchrophasor Estimation in FPGAs: Theory, Implementation, and Validation of a PMU Prototype. *IEEE Trans. Instrum. Meas.* **2014**, *63*, 2824–2836. [CrossRef]
22. Derviškadić, A.; Romano, P.; Paolone, M. Iterative-Interpolated DFT for Synchrophasor Estimation: A Single Algorithm for P- and M-Class Compliant PMUs. *IEEE Trans. Instrum. Meas.* **2018**, *67*, 547–558. [CrossRef]
23. Jin, T.; Zhang, W. A Novel Interpolated DFT Synchrophasor Estimation Algorithm with an Optimized Combined Cosine Self-convolution Window. *IEEE Trans. Instrum. Meas.* **2021**, *70*, 1–10. [CrossRef]
24. Su, T.; Yang, M.; Jin, T.; Flesch, R.C.C. Power Harmonic and Interharmonic Detection Method in Renewable Power Based on Nuttall Double-window All-phase FFT Algorithm. *IET Renew. Power Gener.* **2018**, *12*, 953–961. [CrossRef]
25. Yang, M.; Chen, H. An Interharmonic Detection Method Based on Wavelet Packet and ApFFT. *Prot. Control. Mod. Power Syst.* **2017**, *45*, 112–117.
26. Pan, Y.; Zhang, T.; Zhang, G.; Luo, Z. A Narrowband Anti-Jamming Acquisition Algorithm Based on All-Phase Processing for BOC Signals. *IEEE Access* **2019**, *7*, 41416–41425. [CrossRef]
27. Shao, P.; Zhao, Q.; Guo, H.; Zhang, X. Realization of All Phase-mixed Radix FFT on the Phase Measurement Device. *Power Syst. Prot. Control.* **2016**, *44*, 65–69.
28. Huang, X.; Bai, R.; Zhai, X. All-phase Time-shift Phase Difference Frequency Estimation Based on Frequency Shift Compensation. *J. Tianjin Univ.* **2017**, *50*, 649–655.
29. *IEC/IEEE 60255-118-1:2018*; Measuring Relays and Protection Equipment—Part 118-1:"Synchrophasor for Power Systems—Measurements. IEC: Geneva, Switzerland, 2018; pp. 1–78.